Unusual magnetism in $Cu_xCo_{3-x}O_4$ nanoparticles

M. Shepit [1,*] V. K. Paidi [1] C. A. Roberts,[2] G. K. Reddy,[2] and J. van Lierop [1,3,†]

[1]*Department of Physics and Astronomy, University of Manitoba, Winnipeg, Manitoba, Canada R3T 2N2*

[2]*Toyota Motor Engineering and Manufacturing North America Inc., 1555 Woodridge Avenue, Ann Arbor, Michigan 48105, USA*

[3]*Manitoba Institute for Materials, University of Manitoba, Winnipeg, Manitoba, Canada R3T 2N2*

(Received 27 August 2020; revised 19 November 2020; accepted 24 December 2020; published 28 January 2021)

In Cu-doped Co_3O_4 nanoparticles ($Cu_xCo_{3-x}O_4$; $0 \leqslant x \leqslant 0.5$) Cu occupies both octahedral and tetrahedral sites with a 2+ oxidation state. As the Cu doping increases, we observe changes in the crystal structure corresponding to a Jahn-Teller distortion of the Cu^{2+} sites. To mediate charge balance with Cu^{2+} entering the octahedral sites, a hole forms in the O $2p$ orbitals bonded to the $Cu^{2+}(O_h)$. $Cu^{2+}(T_d)$ is noninteracting and disrupts the existing antiferromagnetic interactions between the $Co^{2+}(T_d)$ ions, while $Cu^{2+}(O_h)$ exhibits a ferromagnetic response as a result of a hybrid form of exchange occurring between $Cu^{2+}(O_h)$ and $Co^{2+}(T_d)$. Emergence of the $3d^9$ ligand hole is directly responsible for the origin of ferromagnetic Cu in the octahedral sites and this results in the unusual magnetism in $Cu_xCo_{3-x}O_4$.

DOI: 10.1103/PhysRevB.103.024448

I. INTRODUCTION

Finite-size effects and broken coordination at the surface lead to a metastable state in magnetic nanoparticles that contributes largely to the overall magnetism [1]. Co_3O_4 is an antiferromagnet with interactions occurring through an extended superexchange pathway [2], thus small changes in the exchange interactions can lead to large changes in the observed magnetism. With Co_3O_4's magnetism well understood, doping with ions such as Cu in the form of binary spinel oxide ($Cu_xCo_{3-x}O_4$) nanoparticles should result in changes to the electronic structure leading to a difference in exchange and overall magnetic properties (e.g., changes in T_N).

$Cu_xCo_{3-x}O_4$ contains divalent Cu ions typically reported as a partially inverted spinel [3,4] where increases in the lattice constant suggest that Cu^{2+} occupies the octahedral sites [4]. The magnetic properties of bulk $Cu_xCo_{3-x}O_4$ ($x \leqslant 1$) have been reported as a weak antiferromagnet with a Néel temperature of $T_N = 18$–24 K [4,5]. Copper has been found to occupy the octahedral site, and this can lead to the possibility of ferromagnetic exchange. To explore the resulting magnetism via a potential change in T_d vs O_h Cu^{2+} ratio from finite-size effects (exchange pathways through surface terminations), phase stable $Cu_xCo_{3-x}O_4$ nanoparticle systems with different dopings were investigated ($0 \leqslant x \leqslant 0.5$).

In pure Co_3O_4, the majority of the exchange strength originates from interactions involving two magnetic $Co^{2+}(T_d)$ ions through two intermediate oxygen ions and a $Co^{3+}(O_h)$, of the form Co^{2+}-O-Co^{3+}-O-Co^{2+}. This exchange pathway occurs in three different configurations, with one ferromagnetic path ($\uparrow\uparrow_{90}$; subscript denotes the 90° O-Co^{3+}-O bond angle) and two antiferromagnetic paths ($\uparrow\downarrow_{90}$, $\uparrow\downarrow_{180}$) [2,6]. The individual interactions for each path are weak; the exchange strength comes from the large multiplicity of the pathways, where we define the multiplicity to be the number of pathways to a neighbor of a given type (e.g., nearest, or next-nearest neighbor). Due to the large distances associated with some of the O^{2-} and $Co^{2+}(T_d)$ ions we find that the typical superexchange interaction only accounts for roughly 10% of the total exchange strength [2,6]. Uniqueness of the exchange pathways $\uparrow\downarrow_{90}$ and $\uparrow\uparrow_{90}$ arise from this small imbalance in the interactions, where Co^{2+}-O-Co^{2+} interactions only occur for nearest neighboring magnetic ions (i.e., $\uparrow\downarrow_{90}$ has an extra component of antiferromagnetic exchange).

When Cu is doped into the Co_3O_4 spinel structure the electronic configuration for the Cu ions in $Cu_xCo_{3-x}O_4$ is altered by the crystal spinel structure causing delocalization of the electrons. Instead of Cu^{3+} occupying the O_h sites, Cu^{2+} resides at the octahedral interstices with a $3d^9\underline{L}$, where $\underline{L}$ denotes a ligand hole on the neighboring oxygen ions. A similar system of magnetic Cu with the feature of hole doping is the cuprates, or hole-doped cuprates. In the hole-doped cuprate compounds, as a substitute for the holes occupying some of the Cu^{2+} creating a mixed valence (Cu^{2+}/Cu^{3+}) structure, the holes tend to occupy the O $2p$ orbitals leaving only Cu^{2+} with $S = 1/2$ [7–9]. In high T_c cuprate compounds, the Cu^{2+} and O ions form CuO_2 planes where the holes in the O $2p$ orbitals then induce the superconductivity [10]. Thus, understanding the nature of the hole on the ligand oxygen ions is critical to our understanding of high T_c superconductors.

$Cu_xCo_{3-x}O_4$ nanoparticles should present entirely new exchange interactions allowing for distinct ferro- and antiferromagnetic behavior. Cu in the spinel structure can undergo a tetragonal distortion caused by the Jahn-Teller effect [3,4,11]; this in turn affects the magnetism through the possible exchange interactions that Cu can undergo. The exchange is investigated through nanoparticles to reveal the dominant magnetism in the structure, where the Cu^{2+} ions in the

*shepitm@myumanitoba.ca

†Johan.van.Lierop@umanitoba.ca

octahedral site and Co^{2+} ions in the tetrahedral site are responsible for the ferromagnetic interactions.

In Co_3O_4, it has been established that substitution of Cu^{2+} into the tetrahedral site leads to a decrease in the strength of the antiferromagnetic exchange that propagates between the (T_d) sites [4,5]. In the cuprate systems, the $3d^9\underline{L}$ ligand hole is responsible for the superconductivity in CuO_2 planes [10]. The ligand hole introduces electron delocalization influencing the conduction and providing a mechanism for the strange ferromagnetic behavior for the involved $Cu^{2+}(O_h)$ ions. The ligand hole permits exchange interactions between the $Cu^{2+}(O_h)$ ($S = 1/2$) and the $Co^{2+}(T_d)$ ($S = 3/2$) through a single oxygen ion. This occurs through a modified exchange interaction involving both double and superexchange resulting in the unusual magnetism of $Cu_xCo_{3-x}O_4$ nanoparticles.

II. EXPERIMENTAL METHODS

The $Cu_xCo_{3-x}O_4$ ($0 \leqslant x \leqslant 0.5$) nanoparticles were synthesized via coprecipitation. Stoichiometric amounts of $Co(NO_3)_3 \cdot 6H_2O$ and $Cu(NO_3)_3 \cdot 2.5\,H_2O$ were dissolved separately in deionized (DI) water and subsequently mixed together for the desired Cu doping. A 2 M NaOH solution is then added dropwise to the stirred solution, and monitored until a *p*H of 9–10 is reached. The precipitate was washed with DI water, filtered, and dried at 120 °C overnight. The samples were then calcined at 500 °C for 1 h, with a heating rate of 2 °C/min to obtain the $Cu_xCo_{3-x}O_4$ nanoparticles.

Transmission electron microscopy (TEM) was performed at the Manitoba Institute for Materials, using a FEI TALOS TEM with an accelerating voltage of 200 keV. Images were processed in IMAGEJ [12].

X-ray diffraction (XRD) was performed with a BRUKER D8 Discover diffractometer with a Cu $K\alpha$ ($\lambda = 1.5405$ Å) x-ray source at a voltage and current of 40 kV and 40 mA, respectively. Patterns were collected from 10° to 90° with a resolution of 0.02° on a rotation stage with a knife edge and Ni $K\beta$ filter.

Magnetic measurements (DC susceptibility) were performed using a Quantum Design MPMS-XL SQUID magnetometer. Samples were mounted in supracil quartz tubes to minimize background interference. DC susceptibility measurements were performed from 2 to 300 K in an applied field of 100 Oe.

O K edge, Co, and Cu L edge x-ray absorption spectroscopy (XAS) and x-ray magnetic circular dichroism (XMCD) were collected using total electron yield (TEY) and total fluorescence yield (TFY) detection at the Advanced Photon Source at Argonne National Laboratory, utilizing the beamline 4-ID-C. Samples were placed on carbon tape mounted on the cold finger of the 70 kOe superconducting magnet and spectra were obtained at 10 K. Co $L_{3,2}$-edge spectra were normalized to the peak at 779.5 eV and O K-edge spectra normalized to the edge jump at 553 eV.

The Co and Cu K-edges x-ray absorption near edge structure (XANES) and extended x-ray absorption fine structure (EXAFS) spectroscopy measurements were performed at beamlines 20-BM-B and 20-ID-C of the Advanced Photon Source at Argonne National Laboratory. The x-ray beam was monochromated by a Si(111) double crystal monochromator

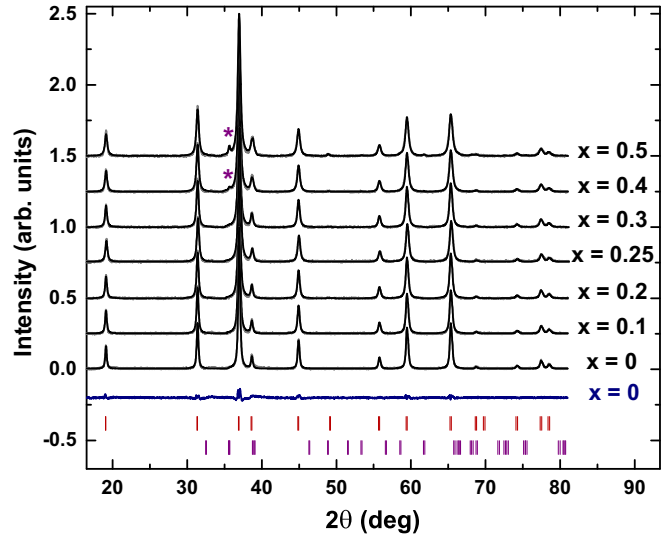

FIG. 1. XRD patterns for all of the samples. Pattern fits (solid black lines), residuals for the $x = 0$ sample (blue line), and peak markers for the primary (red ticks) and secondary CuO phase (*, and purple ticks) are obtained from Rietveld refinements.

where the beam intensity was reduced by 30% to eliminate the higher-order harmonics. Co K-edge measurements were performed in transmission mode and detectors were ionization chamber based. Due to low Cu contents Cu K-edge measurements were done in fluorescence geometry. A 13 element solid-state detector was used to monitor the fluorescence x rays. In both transmission and fluorescence geometries specimens were a thin powder prepared using kapton tape. EXAFS spectra were measured on the Cu-doped Co_3O_4 systems up to $\sim$15 A^{-1} in wave vector k range to analyze the data. XAS spectra are normalized and subtracted using the ATHENA software program, while background subtracted EXAFS spectra were analyzed using the ARTEMIS software [13]. The theoretical calculation of the phase shifts and backscattering amplitudes for specific atom pairs were obtained using the FEFF program [14]. The model used to fit the Cu and Co K-edges data included single scattering paths up to 4 Å (to include first and second coordination shells), and to avoid overparametrization several constraints were included as discussed in the Supplemental Material (SM) [15].

III. RESULTS AND DISCUSSION

A. Structure and composition

XRD is presented for all of the samples in Fig. 1. Rietveld refinements were performed using FULLPROF [16]. Most of the XRD patterns are phase pure with the exception of $x =$ 0.4, 0.5, that present an additional CuO phase of 1% and 3%, respectively. The primary phase is consistent with a spinel structure, with the space group $Fd\bar{3}m$. The refinements show an increase in lattice constant (8.084–8.090 Å) and a decrease in the crystallite size (26–16 nm) across the series as Cu enters the nanoparticles (Fig. 2). The increase in the lattice constant is a result of Cu^{2+} entering the O_h sites due to the difference in ionic radii with Co^{3+} (Cu^{2+}: 0.73 Å; Co^{3+}: 0.55 Å) [4], while the decreased crystallite sizes arise from

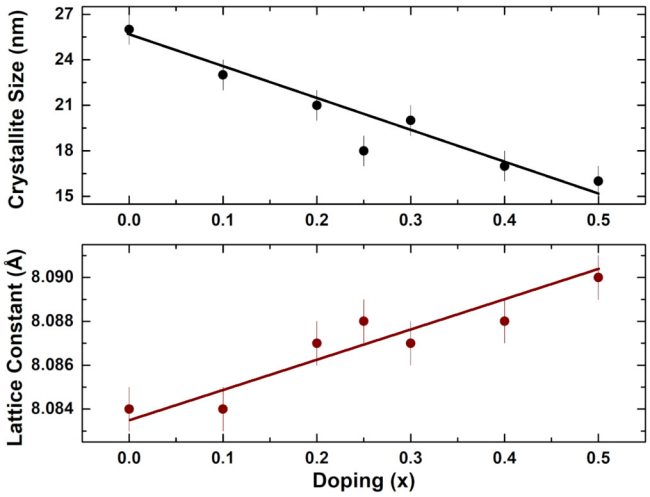

FIG. 2. Crystallite size and lattice constant as a function of doping obtained from XRD refinements. Linear decrease in the crystallite size and increase in the lattice constant as Cu enters the spinel structure.

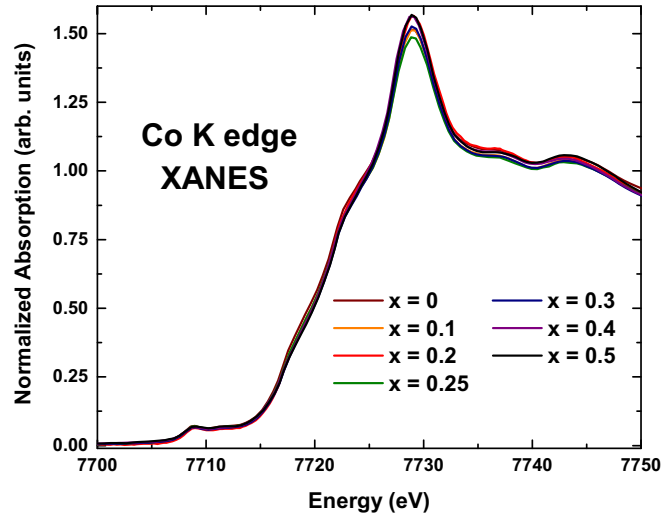

FIG. 3. Co K-edge XANES for all the samples. Spectra were obtained at 300 K.

increased strain within the particles as a result of the Jahn-Teller distortion. Both lattice constant and crystallite size present a linear relationship with Cu doping. From XRD refinements it is found that Cu occupies both octahedral O_h and tetrahedral T_d sites, with an O_h:T_d ratio of roughly 50%:50%. Results from the refinements are presented in Table S.1 in the SM.

Particle sizes (areal averaged) from TEM were obtained from the mean of the lognormal distribution function shown in Table S.2. Volume averaged crystallite sizes from XRD are in decent agreement with the particle sizes obtained from TEM (see SM), indicating that the nanoparticles are consistent with single crystallites.

B. Local environment and cation distribution

XAS measurements were performed over both the Co and Cu K edges. The XANES portion of the spectra allows us to obtain information about the composition while the preedge features contain further information about the $3d$ and $4p$ hybridization in the structure [17,18]. Figure 3 shows the Co K-edge XANES spectra for all the samples, collected at 300 K. We find that all the samples show similar spectra; small changes are found for the edge energies indicating the change in the Co^{2+} to Co^{3+} ratios for the samples. The preedge feature is well defined with two-thirds of the contribution originating from the $1s$ to $3d$ transition of Co(O_h) [17,18]. Since all of the samples show identical preedge features, this is an indication that the O_h:T_d ratios for Co and Cu remain relatively unchanged. For both Co and Cu K edges, there are contributions to the preedge feature arising from the O_h and T_d sites. Normalization of the spectra lead to similar preedge magnitudes indicate identical O_h:T_d ratios between the dopings. The Cu K-edge XANES spectra is shown in Fig. 4 for all the samples. With no change in the edge energy, we find the samples all have a similar overall oxidation state for the Cu ions. The preedge feature is much less defined since the electronic structure of Cu^{2+} ($3d^9$) only allows for one transition per Cu^{2+} to a $3d$ orbital (for both O_h and T_d).

The EXAFS portion of the XAS spectra identifies local changes to the crystal structure around the various cationic species. This allows us to characterize the coordination, interionic distances, bond disorder, and specifically, the occupation of the cationic absorbers. Spectra were taken over the Co and Cu K edges at 300 K to obtain information on how Cu is incorporated into the structure, along with changes to the Co environments as a result of the Cu doping in the nanoparticles. The fitted spectra are shown in Figs. 5 and 6 and the tabulated results and fit parameters for all samples are shown in Tables S.3–S.9 (see SM).

Fits for each sample were performed using the Artemis: EXAFS data analysis software [13]. Fits for the Cu K edge clearly identify the presence of Cu(O_h) and Cu(T_d) as

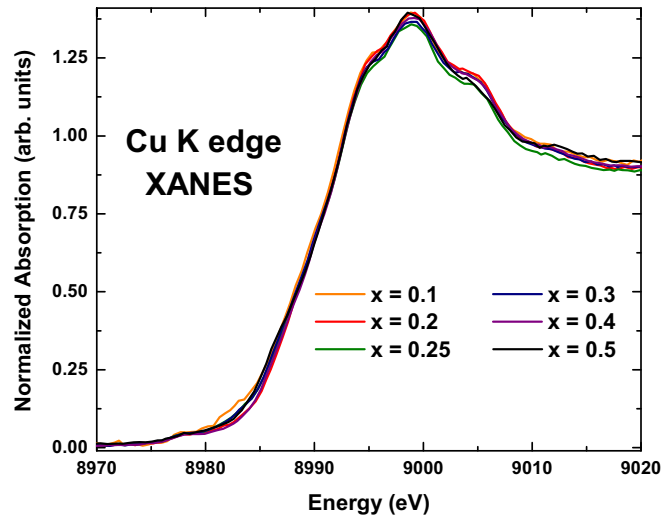

FIG. 4. Cu K-edge XANES of the Cu-doped samples. Spectra were obtained at 300 K. No shift in the edge energy indicates there is no change in the formal Cu oxidation state of the samples.

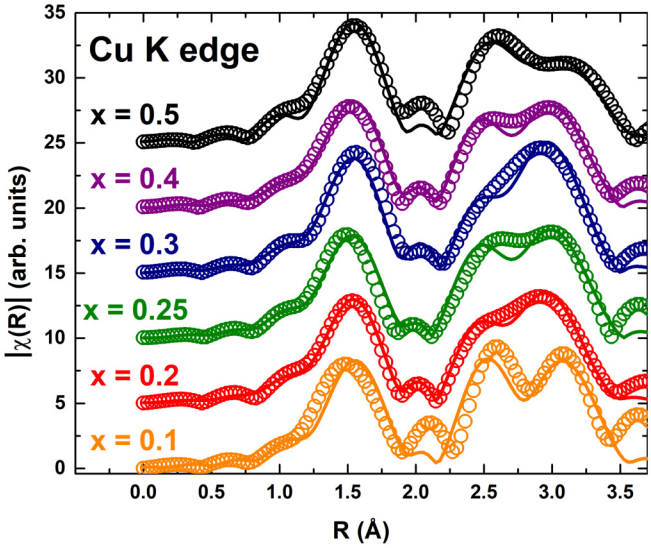

FIG. 5. Cu K-edge EXAFS spectrum for all the samples taken at 300 K. Spectra show changes in the Cu(O_h) and Cu(T_d) occupation.

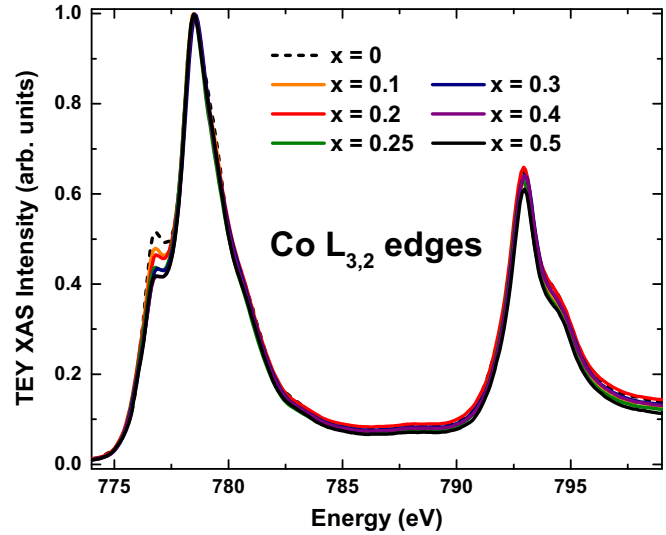

FIG. 7. XAS measurements over the Co $L_{3,2}$ edge obtained at 10 K for all samples. The peak at 777 eV in the Co L-edge spectra show a decrease as Cu enters the structure.

absorbers via the large peaks at 2.6 and 3.2 Å, respectively (Fig. 5). The largest contributions to the peak at 2.6 Å are described by Cu(O_h)-(O_h) scattering events, with Cu(O_h) as the absorber and any (O_h) ion as a scatterer (there are separate contributions from Cu and Co scatterers, but the overlap allows us to characterize the peak as general O_h scattering events). Likewise, the peak at 3.2 Å is a result of the Cu(T_d)-(T_d) paths. For both Co and Cu fits we find that the coordination is as expected for a spinel structure, while scattering path length decreases (as doping increases) for the Co edge, and increases for the Cu edge. Cu causes a shift in the coordination shells, increasing certain distances from Cu absorbers and decreasing the distance to Co absorbers. Intuitively, as doping increases, local disorder (from the Debye-Waller term of the fits) around the Cu ions (σ^2_{Cu}) decreases (or stays the same), while σ^2_{Co} increases. This is evidence of Cu distorting the structure. With enough Cu, this can cause a change in the entire crystal structure of the nanoparticles from cubic to tetragonal [11].

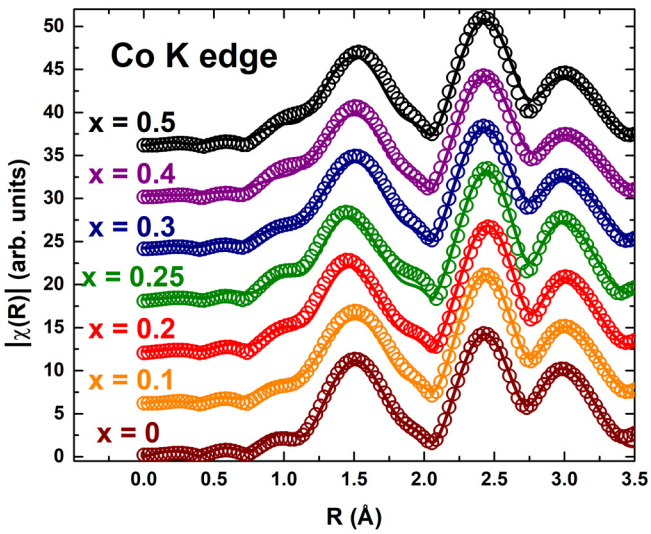

FIG. 6. Co K-edge EXAFS spectrum for all the samples taken at 300 K. Peaks at 2.4 and 3.0 Å are primarily due to the scattering paths of Co(O_h)-(O_h) and Co(T_d)-(T_d), respectively. Solid lines are fits for each doping.

From EXAFS, we have been able to identify the presence of both Cu(O_h) and Cu(T_d) within the spinel structure for each sample. Total Cu in the spinel structure conforms to what was obtained from XRD. Changes in bond distance and bond disorder suggest that doping distorts the crystal structure around Cu. We were also able to identify the presence of CuO (roughly 10%) in the $x = 0.5$ spectrum. The EXAFS results that concern the details of the Cu doping, such as total Cu, Cu(O_h), and Cu(T_d) occupations, and overall chemical formula obtained from EXAFS are shown in Table S.3 (see SM). A detailed description of the EXAFS fitting procedure is also provided in the SM.

L-edge XAS allows us to obtain more specific information regarding the oxidation state and the environment of the cations and surrounding oxygen atoms. Figure 7 shows the XAS spectra at 10 K for all of the samples over the Co $L_{3,2}$ edges. The Co L-edge spectra are typical of a Co_3O_4 spinel-type material [19]. The decrease in the shoulder at 777 eV indicates a decrease in the occupation of the Co sites. The peak at 777 eV is dominated by $Co^{2+}(T_d)$, but small contributions from $Co^{3+}(O_h)$ are also present. Figure 8 shows a close-up of the Co L_3 edge, where I_{2+} and I_{3+} indicate the intensities of the $Co^{2+}(T_d)$ and $Co^{3+}(O_h)$ contributions. The inset shows I_{3+}/I_{2+} increasing as a function of Cu doping, indicating the change in relative occupancies.

The Cu $L_{3,2}$-edge spectra obtained at 10 K for the Cu-doped nanoparticles (Fig. 9) are indicative of Cu^{2+} ions [21–24]. The small shoulder peak at 932.5 eV is due to the existence of a ligand hole ($2p3d^9\underline{L} \rightarrow 2p^5 3d^9$) that arises from the O_h sites: $Cu^{3+}(O_h) \rightarrow Cu^{2+}(O_h) + 3d^9\underline{L}$ as Cu prefers a 2+ oxidation state over a 3+ oxidation state [10,25,26]. The $3d^9\underline{L}$ mediates charge balance in the structure allowing Cu^{2+}

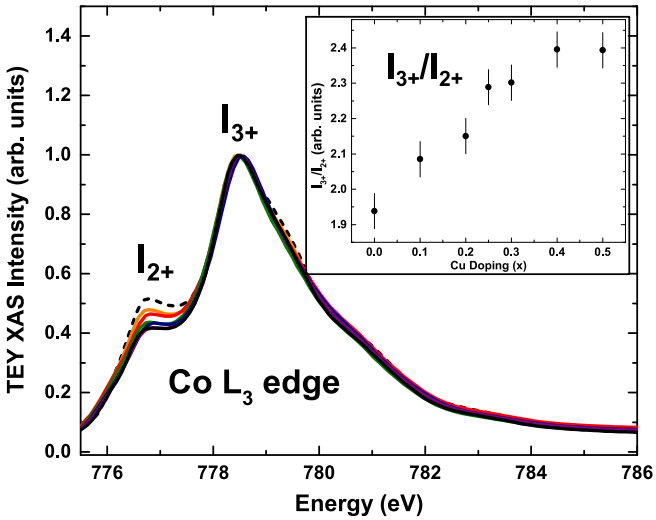

FIG. 8. XAS measurements showing only the Co L_3 edge. I_{2+} and I_{3+} are the intensities for the $Co^{2+}(T_d)$ and $Co^{3+}(O_h)$ contributions. The inset shows I_{3+}/I_{2+} vs doping.

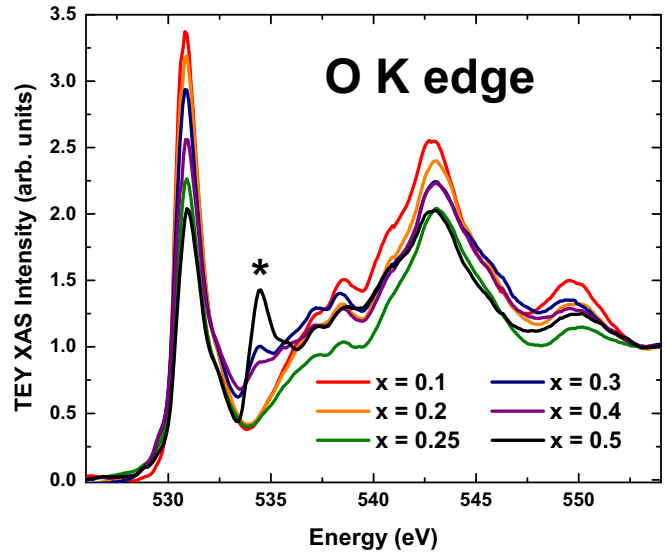

FIG. 10. XAS obtained over the O K edge for all samples. Changes in the 3d occupation between the samples is indicated by the changes in the preedge peak at 532 eV. The asterisk (*) marks the peak from vicinal oxygen [20].

to exist in both the O_h and T_d sites, without Co^{3+} entering the T_d sites. The $3d^9\underline{L}$ causes a change in the electronic wave functions due to the O ions collectively lacking an electron.

O K-edge XAS allows us to probe the hybridization between O 2p and metal 3d and 4s states directly. The oxygen K-edge spectra shown in Fig. 10 were taken at 10 K for all samples. The preedge peak at 531.5 eV and the shoulder at 533 eV allow us to quantify the 3d e_g and t_{2g} orbital occupation for the O_h ions in the structure [27]. The occupation of these orbitals conforms to what we expect if Cu replaces Co in the O_h site, thus providing another method to confirm the presence of $Cu^{2+}(O_h)$. With Co^{3+} containing four e_g vacancies and Cu^{2+} containing only one vacancy in the e_g orbital, we expect a decrease in the absorption across the series. There is also a decrease in the absorption above the threshold in the region of 537–552 eV. This is due to the decrease in hybridization between O p and cationic 4s states, as a result of Cu^{2+} occupying both sites. $Cu^{2+}(O_h)$ still undergoes hybridization with the O ligand orbitals, but $Cu^{2+}(T_d)$ ions do not hybridize with O orbitals.

It is known that the separation of the $Cu^{2+}(T_d)$ and $Cu^{2+}(O_h)$ absorptions is only 0.7 eV [28]. Thus, to further examine the Cu spectra, a peak deconvolution is performed on the main absorption for the Cu L_3 edge to obtain a third estimate of the T_d and O_h occupancies (Fig. 11 shows $x = 0.2$). We find that the T_d occupation is always greater than the octahedral occupation (omitting $x = 0.1$), with a magnitude of

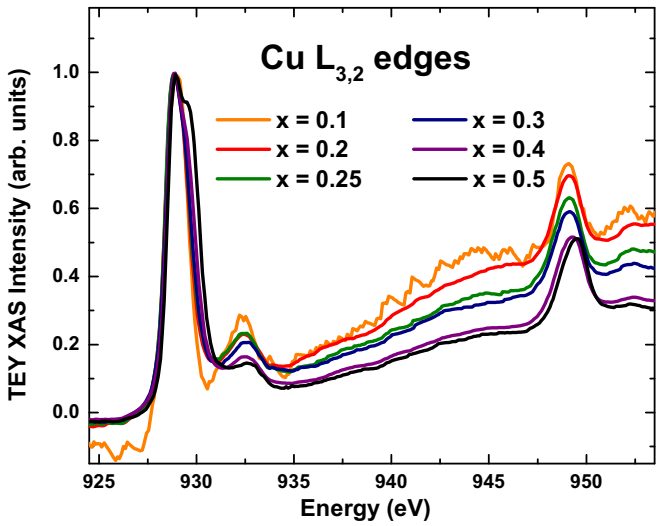

FIG. 9. XAS measurements over the Cu $L_{3,2}$ edge obtained at 10 K for all samples. Cu L-edge spectra are all very similar. The $x = 0.5$ sample shows another absorption due to the CuO impurity phase.

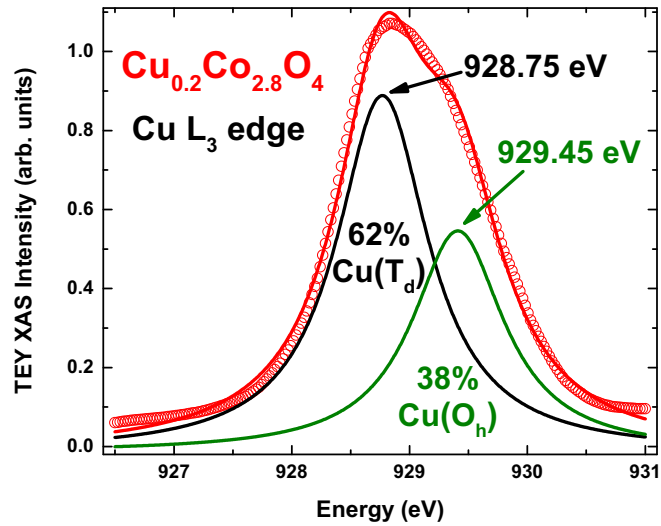

FIG. 11. Fit for the Cu L_3 edge for the $x = 0.2$ sample. With a separation of 0.7 eV for the $Cu^{2+}(O_h)$ and $Cu^{2+}(T_d)$ absorptions, we find 38% of the Cu occupies O_h sites and 62% occupies T_d sites.

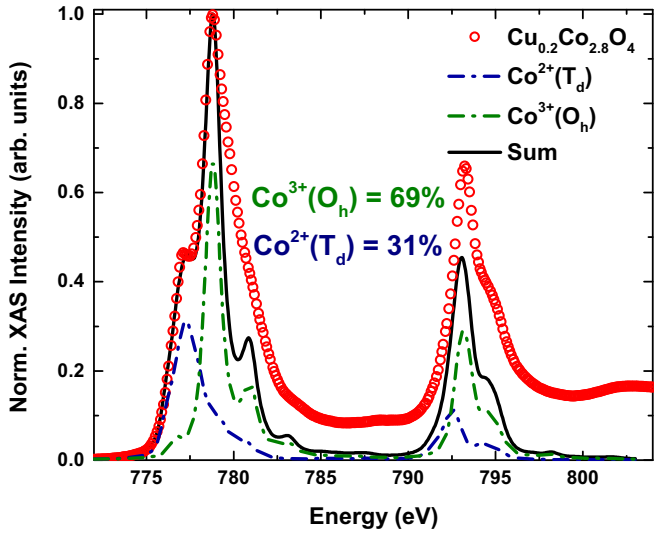

FIG. 12. Fit for the Co $L_{3,2}$-edge spectra for the $x = 0.2$ sample shows the absorption at 777 eV is dominated by Co^{2+} but contains small contributions from Co^{3+} ions.

roughly 60%–65%. As the Cu doping increases ($x \geqslant 0.4$), the emergence of a third absorption becomes resolvable within the Cu L_3-edge peak. This is attributed to the formation of the CuO impurity phase; for $x = 0.5$ an impurity of ~7% was found. We were also able to obtain fits for the Co L-edge spectra. Fits for the Co edge were obtained by simulations of the $Co^{2+}(T_d)$ and $Co^{3+}(O_h)$ contributions using CTM4XAS [29]. The fit for $x = 0.2$ is shown in Fig. 12, where the $Co^{3+}(O_h)$ and $Co^{2+}(T_d)$ occupations are 69% and 31%, respectively.

The results for the occupancies of the nanoparticles obtained from the Co and Cu L-edge XAS fits are shown in Fig. 13. We find that the occupation of $Cu^{2+}(T_d)$:$Cu^{2+}(O_h)$ remains the same at roughly 60%:40%. This is corroborated

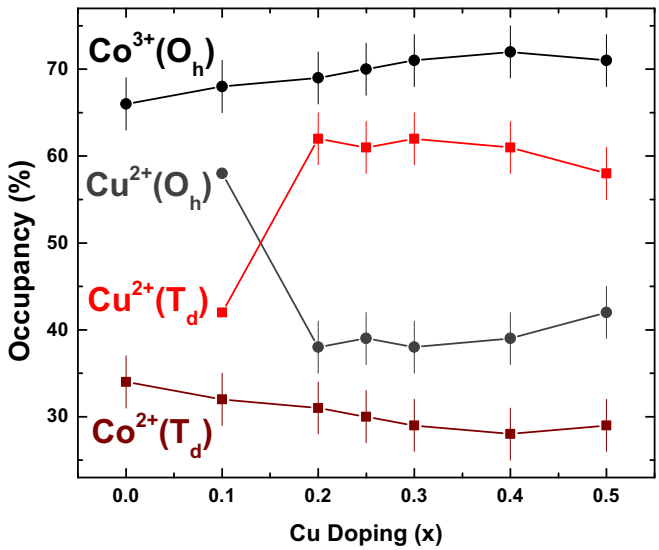

FIG. 13. Occupancies obtained from fits of the Co and Cu L-edge XAS. There is an increase in the $Co^{3+}(O_h)$ occupancy results from the decrease in $Co^{2+}(T_d)$ occupancy. $Cu^{2+}(T_d)$ occupancy is constant at 60% (excluding $x = 0.1$).

by the height of the $3d^9\underline{L}$ (Fig. 9); if we take into account the backgrounds, the height of the high-energy shoulder peak is nearly identical throughout the series. Since we obtain the same ratio of ligand core holes that arise from Cu(O_h), we obtain the same ratio for Cu(O_h) and Cu(T_d) between the dopings. Cu occupancies and total Cu are roughly in agreement with the results from both XRD and EXAFS. The tabulated L-edge XAS results are shown in Table S.10, along with fit parameters for the Co L-edge simulations in Table S.11 (see SM).

From XAS we have identified the oxidation states and obtained accurate estimations of the O_h and T_d occupancies for the cations in the structure. All of the samples show very similar spectra with a Cu(T_d) occupancy larger than the Cu(O_h) occupancy. XAS and EXAFS can also be used to verify that the structure is being doped with Cu, and not a surface substitution. XAS over the Co and Cu L edges was performed with both TEY detection and TFY detection. EXAFS is performed in a transmission geometry setup probing both the surface and the core of the nanoparticles; while TFY XAS mostly probes the core of the particles, TEY only probes the first few nanometers [30]. This gives us a good distinction between the core and surface, allowing us to distinguish different contributions from the core and surface [31]. TFY XAS measurements also clearly show the Cu entering the core of the structure (see SM).

C. Magnetism and exchange properties

For antiferromagnets such as Co_3O_4 the maximum in the DC susceptibility $\chi(T)$ is a typical identifier of the Néel temperature (T_N). Further, examination of the susceptibility above and below the ordering temperature gives us an indication of the exchange interactions present. To investigate the effects of the Cu doping on the magnetism of cobalt oxide nanoparticles we performed low-field DC susceptibility for all of the Cu-doped Co_3O_4 samples (shown in Fig. 14).

It is known that for bulk Co_3O_4 $T_N = 40$ K [2,6]. As the Cu doping increases, we observe a decrease in T_N. This is a result of the complicated nature of the exchange interactions in Co_3O_4. The majority of the exchange strength arises from multiple extended superexchange interactions, leading to the magnetic structure shown in Fig. 15. The extended superexchange pathways are fairly weak but each pathway has a large number of possible iterations, i.e., multiplicity. The three paths in the figure use the notation $\uparrow\uparrow$ and $\uparrow\downarrow$ to denote ferro- and antiferromagnetic interactions, while the subscript denotes the O-Co^{3+}-O bond angle. With essentially noninteracting Cu in the tetrahedral site, it then becomes clear why we see a decrease in the magnetic ordering when Cu^{2+} occupies the T_d site.

In pure Co_3O_4 the $\uparrow\uparrow_{90}$ and $\uparrow\downarrow_{90}$ exchange paths have the same bond angles and bond distances, thus to first order their interaction strengths cancel [2,6]. But this is not the case for the Cu-doped samples. As Cu enters the structure changes in the ionic radii and unit cell lead to changes in the bond distances and bond angles for the exchange interactions. This leads to the possibility for an asymmetry in the $\uparrow\downarrow_{90}$ and $\uparrow\uparrow_{90}$ interactions such that cancellation between these two exchange paths may not occur in all cases, as in pure Co_3O_4.

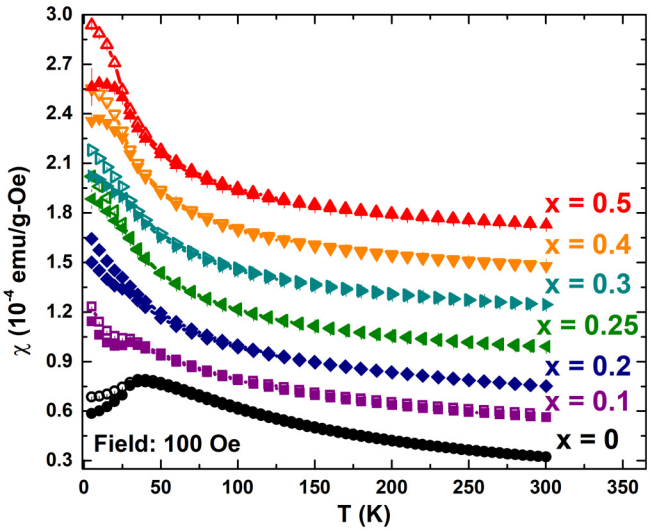

FIG. 14. $\chi(T)$ for all of the dopings shows a decrease in the ordering temperature with increasing Cu doping. Below the ordering temperature we find evidence of ferromagnetic behavior as the doping increases.

Above the magnetic ordering temperature the samples are all paramagnetic. This allows us to represent the susceptibility by a modified Curie-Weiss law $\chi(T) = \chi_0 + \frac{C}{T-\theta}$. Where χ_0 is the temperature independent susceptibility, C is the Curie constant, and θ is the Weiss temperature. The magnetic moment and exchange can be quantified from an analysis of the inverse in DC susceptibility $[1/\chi(T)$; see SM]; high temperature fits were performed for all samples with the results displayed in Table S.12.

The temperature independent susceptibility χ_0 is a result of the van Vleck paramagnetism from the different ionic species showing virtually no change throughout the series [32]. θ gives us an idea of the exchange interactions present, with $\theta < 0$ indicating antiferromagnetic exchange; bulk values for θ for Co_3O_4 range from -50 to -110 K [2,33–35]. The

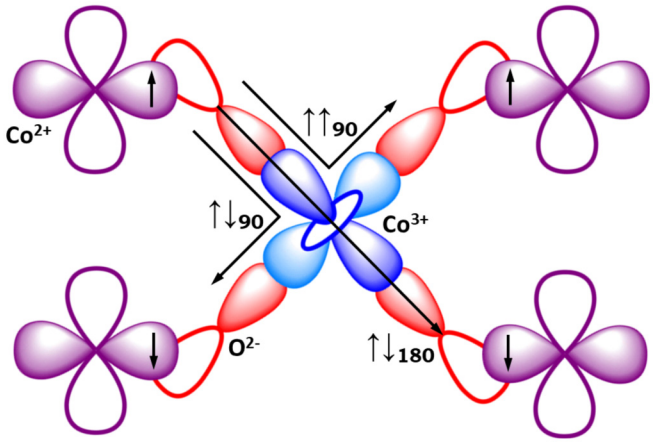

FIG. 15. The three different exchange pathways present in Co_3O_4 are shown: $\uparrow\uparrow_{90}$, $\uparrow\downarrow_{90}$, and $\uparrow\downarrow_{180}$ (subscript denotes O-Co^{3+}-O bond angle). $\uparrow\uparrow_{90}$ and $\uparrow\downarrow_{90}$ have the same bond angles and bond distances, thus to a first order, these interactions cancel.

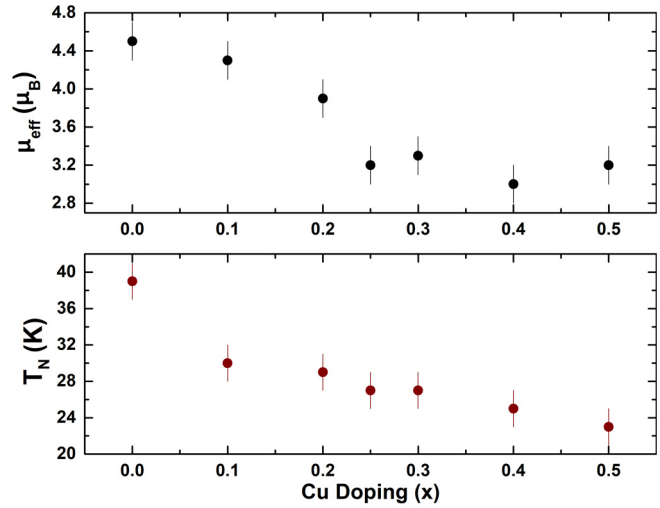

FIG. 16. μ_{eff} and T_N obtained from the fits of $1/\chi(T)$ as a function of the nominal Cu doping. Both μ_{eff} and T_N show a decrease with an increasing Cu.

samples show a decrease in θ with doping, indicating a decrease in the antiferromagnetic exchange interactions. The Curie constant C provides us with a quantitative measure of the overall magnetic moment $(2.83\times\sqrt{C_{\text{mol}}})$. Figure 16 shows the values of μ_{eff} obtained from fits of $1/\chi(T)$ and T_N obtained from the peak in DC susceptibility as a function of the Cu doping. We find that there is a decrease in the overall magnetic moment and a decrease in the ordering temperature corresponding to the decrease in Co occupancies. The decrease in μ_{eff} results from the decrease in $Co^{2+}(T_d)$, while the decrease in T_N is a consequence of the decreasing multiplicity in the antiferromagnetic exchange interactions.

To gain further insight, we investigate J_{ij} [36] and θ as a function of doping for the nanoparticles, shown in Fig. 17. We find that both the exchange constant and Weiss

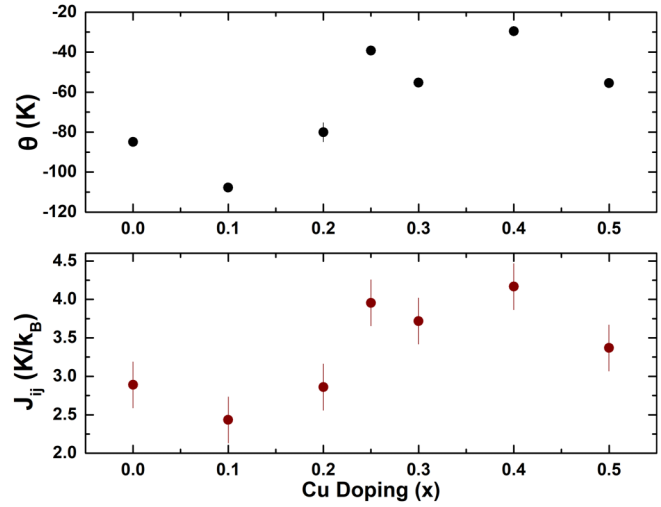

FIG. 17. θ and J_{ij} as a function of doping obtained from magnetometry. Both θ and J_{ij} show identical behavior, increasing as doping increases. This is a result of the decrease in antiferromagnetic interactions.

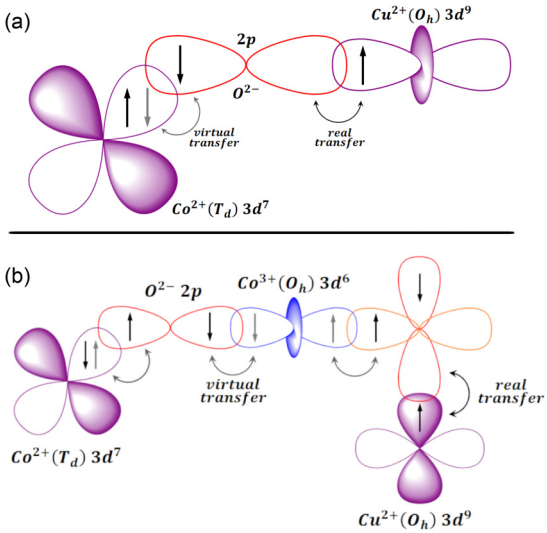

FIG. 18. (a) Stronger ferromagnetic exchange interactions occur between $Co^{2+}(T_d)$ and $Cu^{2+}(O_h)$ ions, involving both double and superexchange. (b) The antiferromagnetic extended superexchange interaction between $Co^{2+}(T_d)$ and $Cu^{2+}(O_h)$ is much weaker.

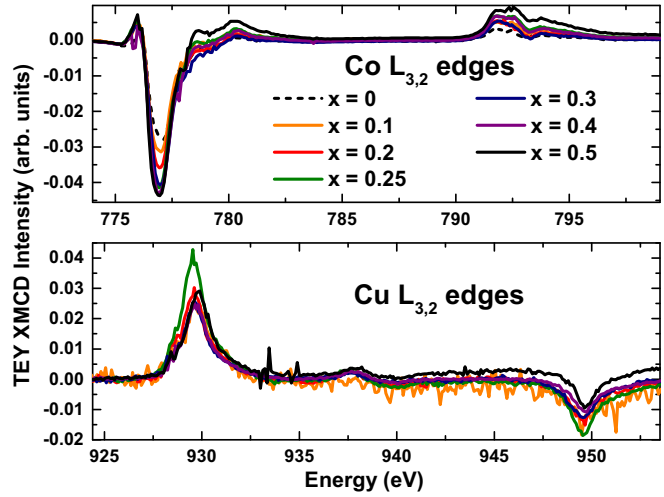

FIG. 19. Co and Cu L-edge XMCD obatained at 10 K. The Co L edge shows an increase in the magnetic moment due to the weakening antiferromagnetic interactions. The Cu L-edge XMCD shows an unchanging magnetic moment present only on the Cu(O_h) site.

temperature show identical behavior. The increase in the exchange constant J_{ij} and θ with doping is consistent with the decrease in antiferromagnetic interactions. θ is obtained directly from the fit and J_{ij} is described by both T_N (not obtained from fit) and μ_{eff} (obtained from fit), thus J_{ij} and θ are independent methods in confirming the exchange interactions present. The decrease in both J_{ij} and θ for the $x = 0.5$ sample is due to the appearance of the CuO impurity phase. The total Cu(T_d) occupation follows roughly the same tenancy as both the exchange and Weiss temperature.

As temperature decreases the susceptibility of the dopings increases more rapidly with Cu, and $\chi(T)$ below the magnetic ordering T_N shows evidence of weak ferromagnetic interactions. This is a result of the addition of Cu into the O_h sites. Weak ferromagnetic interactions occur between $Co^{2+}(T_d)$-$Cu^{2+}(O_h)$, made possible only by the $3d^9$ ligand hole on the intermediate oxygen ions. The ligand hole allows for the propagation of magnetic interactions via specialized exchange interactions involving both double (real transfer of electrons) and superexchange (virtual transfer of electrons) interactions [shown in Fig. 18(a)]. In addition to the ferromagnetic exchange interactions between $Co^{2+}(T_d)$ and $Cu^{2+}(O_h)$, an antiferromagnetic extended superexchange interaction exists, similar to the form of the exchange in nominal Co_3O_4 that involves three intermediate ions [Fig. 18(b)]. Due to the extended nature of exchange the antiferromagnetic interactions between $Co^{2+}(T_d)$ and $Cu^{2+}(O_h)$ are much weaker.

The most straightforward evidence of ferromagnetic interactions occurring in the particles is the XMCD. XMCD uses both left and right circularly polarized x rays to measure both spin-up and spin-down populations. Intrinsically, XMCD is not observable for antiferromagnets. XMCD spectra were measured by reversing the x-ray polarization at each energy interval and then the applied magnetic field polarity (±50 kOe; to permit any artifacts intrinsic to the x-ray scattering processes to be removed from the resulting XMCD spectra—"artifact-free" XMCD). Co and Cu L-edge XMCD obtained at 10 K is shown in Fig. 19. For the Co L-edge XMCD, due to the nonmagnetic nature of the Co^{3+} ion, there is only a contribution from Co^{2+} ions. The Co L_3-edge peak (777 eV) shows an increase in the dichroic signal with doping, resulting from the increase in moment for the Co^{2+} ions. This is due to the decrease in antiferromagnetic and increase in ferromagnetic interactions directly related to $Co^{2+}(T_d)$. Expectedly, in the Cu L-edge XMCD we find a maximum occurring at ~929 eV indicating the moment originates from the $Cu^{2+}(O_h)$ ion. Because $Cu^{2+}(T_d)$ is noninteracting, exchange interactions of the form $Cu^{2+}(T_d)$-O-Co^{3+}-O-Co^{2+} are nonexistent.

XMCD is the clearest way to show the ferromagnetic behavior that arises from the interactions between the $Co^{2+}(T_d)$ and the $Cu^{2+}(O_h)$ ion via the double exchange interaction. This is made possible by the ligand hole created on the intermediate O ions. From the Cu L-edge XMCD the magnetic moment between the dopings is virtually unchanged; this results from the constant occupancies of Cu(O_h) and Cu(T_d) since the XMCD is XAS normalized. Thus, as the doping increases, the occupancy of each site increases equally; this increases the XAS and XMCD proportionally, thus normalizing to the same magnetic moment. Stated differently, this means there is no change to the individual magnetic interactions between $Cu^{2+}(O_h)$ and $Co^{2+}(T_d)$.

Using CTM4XAS we can simulate the XMCD spectrum for the Co L edge. The simulation of the $x = 0.2$ sample is shown in Fig. 20. Since $Co^{2+}(T_d)$ presents the only contribution in the XMCD across the Co L edge, the XMCD simulations for each sample agree well with what we have obtained experimentally. Due to the decrease in antiferromagnetic interactions the magnetic moment of the $Co^{2+}(T_d)$ for the $x = 0.2$ sample is ~1.2 times larger than the magnetic moment obtained from Co_3O_4.

Using XMCD we are able to link the characterization of the crystal structure to the magnetism. It was found that

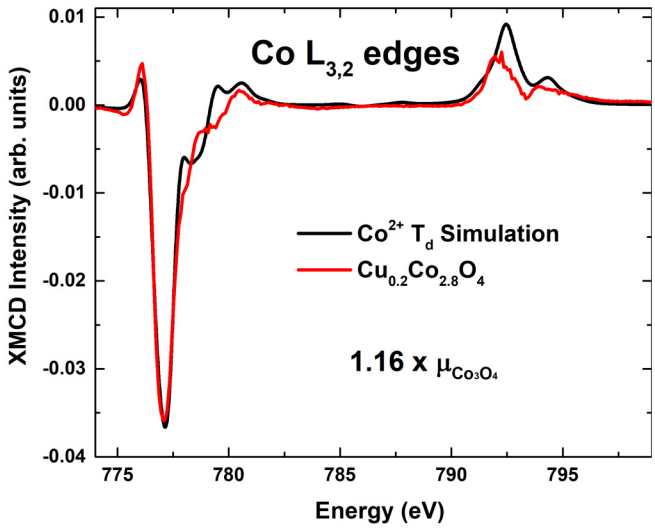

FIG. 20. Co L-edge XMCD fit for the spectrum obtained at 10 K for the $x = 0.2$ sample. Due to the electronic structure of the Co^{3+} ions, there is only a magnetic moment for the $Co^{2+}(T_d)$ ion. For $x = 0.2$ the magnetic moment is ~1.2 times larger than Co_3O_4.

$Cu^{2+}(T_d)$ undergoes no hybridization with O ions leading to no magnetic interactions, as expected from the analysis of the susceptibility [there is a possibility that $Cu^{2+}(T_d)$ provides a very weak antiferromagnetic interaction with $Co^{2+}(T_d)$, but this is much weaker than the original exchange between $Co^{2+}(T_d)$ ions [4,5]]. And as a result, $Cu^{2+}(T_d)$ disrupts the existing ferro- and antiferromagnetic interactions that occur between the $Co^{2+}(T_d)$ ions. This is indicated by the increased magnetic moment on the $Co^{2+}(T_d)$ obtained from Co L-edge XMCD fits. Ferromagnetic interactions are found to occur between the $Co^{2+}(T_d)$ and $Cu^{2+}(O_h)$; while antiferromagnetic interactions between the two ions are also possible, the extended nature results in dominant ferromagnetic interactions. The $3d^9$ ligand hole created as a consequence of Cu occupying the octahedral site provides the mechanism for exchange to occur through the O $2p$ orbitals. The hybridization that ensues between the $Cu(O_h)$ and O $2p$ orbitals results in ferromagnetic Cu.

IV. CONCLUSIONS

We have used XRD, EXAFS, and XAS to obtain information about the crystal structure of Cu-doped Co_3O_4, which is then used to evaluate the magnetic structure. It has been found that Cu occupies both O_h and T_d sites in the structure, with a preference for the Cu to occupy the T_d sites. We find that the Cu in the spinel structure occupies cationic sites with an O_h:T_d ratio of roughly 40%:60%. XRD, EXAFS, and XAS are all in agreement concerning the total Cu content, CuO impurity phase, and $Cu(O_h)$ and $Cu(T_d)$ occupancies.

From L-edge XAS, we find that Cu occupies both O_h and T_d sites with a 2+ oxidation state. This occurs because Cu prefers a 2+ oxidation state and, as a result, the $Cu^{2+}(O_h)$ form a $3d^9$ ligand hole [$Cu^{3+}(O_h) \rightarrow Cu^{2+}(O_h) + 3d^9\underline{L}$]. From XRD, the Cu-doped structure shows increased strain and EXAFS shows increased disorder and changes to the scattering path lengths. This is consistent with Cu distorting the structure.

Magnetic measurements show that $Cu^{2+}(T_d)$ is noninteracting and as expected, disrupts the preexisting exchange interactions occurring between $Co^{2+}(T_d)$ ions. From XMCD, it is found that $Cu^{2+}(O_h)$ undergoes ferromagnetic interactions. $Cu^{2+}(O_h)$ induces a $3d^9$ ligand hole which causes hybridization between the $Cu^{2+}(O_h)$ and O ions; this provides the mechanism for ferromagnetic exchange interactions occurring between $Co^{2+}(T_d)$ and $Cu^{2+}(O_h)$. The increased ferromagnetic interactions and decreased antiferromagnetic interactions result in an increase in the overall magnetization for the Cu-doped particles. The newly introduced ferromagnetic interactions occur via a hybrid double and superexchange interaction Co^{2+}-O-$Cu^{2+}(O_h)$. The antiferromagnetic superexchange interactions between $Co^{2+}(T_d)$ ions, and the mixed exchange interactions between $Co^{2+}(T_d)$ and $Cu^{2+}(O_h)$ create the unusual magnetism that shows both ferro- and antiferromagnetic behavior.

Data presented in Ref. [37] differs slightly due to new considerations in the Cu structure. This does not affect the analysis presented in the previously published paper.

ACKNOWLEDGMENTS

The authors thank Dr. Freeland and Dr. Brewe from the Advanced Photon Source at Argonne National Laboratory for aid with the x-ray absorption spectroscopy. The authors also thank the National Science and Engineering Research Council of Canada (NSERC) Grant No. RGPIN-2018-05012 and the Canadian Foundation for Innovation (CFI) for their financial support throughout this work. This research used resources of the Advanced Photon Source, a US Department of Energy (DOE) Office of Science User Facility, operated for the DOE Office of Science by Argonne National Laboratory under Contract No. DE-AC02-06CH11357.

[1] A. Balan, P. M. Derlet, A. F. Rodríguez, J. Bansmann, R. Yanes, U. Nowak, A. Kleibert, and F. Nolting, Phys. Rev. Lett. **112**, 107201 (2014).

[2] W. L. Roth, J. Phys. Chem. Solids **25**, 1 (1964).

[3] A. La Rosa-Toro, R. Berenguer, C. Quijada, F. Montilla, E. Morallón, and J. L. Vázquez, J. Phys. Chem. B **110**, 24021 (2006).

[4] S. Angelov, E. Zhecheva, K. Petrov, and D. Menandjiev, Mater. Res. Bull. **17**, 235 (1982).

[5] M. Shimada, F. Kanamaru, M. Koizumi, and N. Yamamoto, Mater. Res. Bull. **10**, 733 (1975).

[6] W. Roth, J. Phys. France **25**, 507 (1964).

[7] J. A. Yarmoff, D. R. Clarke, W. Drube, U. O. Karlsson, A. Taleb-Ibrahimi, and F. J. Himpsel, Phys. Rev. B **36**, 3967 (1987).

[8] N. Nücker, J. Fink, J. C. Fuggle, P. J. Durham, and W. M. Temmerman, Phys. Rev. B **37**, 5158 (1988).

[9] C. T. Chen, F. Sette, Y. Ma, M. S. Hybertsen, E. B. Stechel, W. M. C. Foulkes, M. Schluter, S.-W. Cheong, A. S. Cooper, L. W. Rupp, B. Batlogg, Y. L. Soo, Z. H. Ming, A. Krol, and Y. H. Kao, Phys. Rev. Lett. **66**, 104 (1991).

[10] G. Sawatzky and R. Green, *Quantum Materials: Experiments and Theory* (Autumn School on Correlated Electrons, Jülich, 2016).

[11] G. Dionne, *Magnetic Oxides* (Springer, New York, 2009), pp. 1–466.

[12] C. T. Rueden, J. Schindelin, M. C. Hiner, B. E. DeZonia, A. E. Walter, E. T. Arena, and K. W. Eliceiri, arXiv:1701.05940v4.

[13] B. Ravel and M. Newville, J. Synchrotron Radiat. **12**, 537 (2005).

[14] J. J. Rehr and R. C. Albers, Rev. Mod. Phys. **72**, 621 (2000).

[15] See Supplemental Material at http://link.aps.org/supplemental/10.1103/PhysRevB.103.024448 for data and fitting procedures relevant to the manuscript.

[16] J. Rodríguez-Carvajal, Phys. B: Condens. Matter **192**, 55 (1993).

[17] C. H. M. van Oversteeg, H. Q. Doan, F. M. F. de Groot, and T. Cuk, Chem. Soc. Rev. **46**, 102 (2017).

[18] M. L. Baker, M. W. Mara, J. J. Yan, K. O. Hodgson, B. Hedman, and E. I. Solomon, Coord. Chem. Rev. **345**, 182 (2017).

[19] F. Morales, F. M. F. de Groot, P. Glatzel, E. Kleimenov, H. Bluhm, M. Hävecker, A. Knop-Gericke, and B. M. Weckhuysen, J. Phys. Chem. B **108**, 16201 (2004).

[20] F. Lin, D. Nordlund, T. Pan, I. M. Markus, T.-C. Weng, H. L. Xin, and M. M. Doeff, J. Mater. Chem. A **2**, 19833 (2014).

[21] P. Zhang, L. Li, D. Nordlund *et al.*, Nat. Commun. **9**, 381 (2018).

[22] A. Sharma, M. Varshney, J. Park, T.-K. Ha, K.-H. Chae, and H.-J. Shin, RSC Adv. **5**, 21762 (2015).

[23] P. Jiang, D. Prendergast, F. Borondics, S. Porsgaard, L. Giovanetti, E. Pach, J. Newberg, H. Bluhm, F. Besenbacher, and M. Salmeron, J. Chem. Phys. **138**, 024704 (2013).

[24] C. Prajapat, S. Singh, D. Bhattacharya *et al.*, Sci. Rep. **8**, 3732 (2018).

[25] D. Meyers, S. Mukherjee, J.-G. Cheng, S. Middey, J.-S. Zhou, J. Goodenough, B. Gray, J. Freeland, T. Saha-Dasgupta, and J. Chakhalian, Sci. Rep. **3**, 1834 (2013).

[26] M. Magnuson, T. Schmitt, V. N. Strocov, J. Schlappa, A. S. Kalabukhov, and L. C. Duda, Sci. Rep. **4**, 7017 (2014).

[27] F. M. F. de Groot, M. Grioni, J. C. Fuggle, J. Ghijsen, G. A. Sawatzky, and H. Petersen, Phys. Rev. B **40**, 5715 (1989).

[28] K. Shimizu, H. Maeshima, H. Yoshida, A. Satsuma, and T. Hattori, Jpn. J. Appl. Phys. **38**, 44 (1999).

[29] E. Stavitski and F. M. F. de Groot, Micron (Oxford, England: 1993) **41**, 687 (2010).

[30] R. Nakajima, J. Stöhr, and Y. U. Idzerda, Phys. Rev. B **59**, 6421 (1999).

[31] S. Sambasivan, D. A. Fischer, B. M. DeKoven, and A. Kuperman, Adv. Mater. **12**, 1809 (2000).

[32] P. Cossee, in *Proceedings of the International Symposium on the Chemistry of the Co-ordination Compounds* [J. Inorg. Nucl. Chem. **8**, 483 (1958)].

[33] P. Dutta, M. S. Seehra, S. Thota, and J. Kumar, J. Phys.: Condens. Matter **20**, 015218 (2007).

[34] Co_3O_4: magnetic properties, in *Non-Tetrahedrally Bonded Binary Compounds II*, edited by O. Madelung,U. Rössler, M. Schulz, Landolt-Börnstein - Group III Condensed Matter Vol. 41D (Springer-Verlag, Berlin/Heidelberg, 2000).

[35] S. A. Makhlouf, J. Magn. Magn. Mater. **246**, 184 (2002).

[36] S. Blundell, *Magnetism in Condensed Matter*, Oxford Master Series in Condensed Matter Physics (Oxford University Press, Oxford, 2001).

[37] C. A. Roberts, V. K. Paidi, M. Shepit, T. C. Peck, K. L. Stamm Masias, J. van Lierop, and G. K. Reddy, Catal. Today **360**, 204 (2021).